JMEPEG (2022) 31:5697–5705
https://doi.org/10.1007/s11665-022-06675-x

1059-9495/$19.00

TECHNICAL ARTICLE

Microstructural Stability and Mechanical Property of a Medium-Si 12%Cr Reduced Activation Ferritic/Martensitic Steel at High Temperatures

Sen Ge, Ben Niu, Zhenhua Wang, Qianfu Pan, Chaohong Liu, and Qing Wang

Submitted: 14 November 2021 / Revised: 17 January 2022 / Accepted: 29 January 2022 / Published online: 22 February 2022

The present work investigated the microstructural stability and mechanical property of a medium-Si 12%Cr reduced activation ferritic/martensitic steel (Fe-0.21C-11.76Cr-1.41W-0.17Ta-0.2V-0.63Si-0.51Mn-0.015N, wt.%) at high temperatures. Alloy samples were normalized at 1100 °C for 1 h and tempered at 700 ºC for 1 h, and finally aged at 550 and 650 °C for 5-500 h. In the tempered state, $Cr_{23}C_6$ and MC carbides were precipitated into the full martensitic matrix, which is consistent with the thermodynamic calculated results. This alloy exhibited a higher microstructural stability during aging at 550 ºC without any obvious widening of martensitic laths and coarsening of carbides. But the martensitic laths were widened when aged at 650 ºC, as evidenced by the increase in lath width from ~ 124 nm in tempered state to ~ 275 nm in 500 h-aged state. Also, the $Cr_{23}C_6$ carbides were coarsened with the length increasing from ~ 132 nm in tempered state to ~ 240 nm in 500 h-aged state along the lath interface. While MC carbides have a much higher stability and the particle size keeps constant (90-110 nm) even after 500 h aging at 650 ºC, which is ascribed to the different diffusion coefficients of carbide-forming elements. This aged alloy exhibited prominent mechanical properties with high yield strength of σ_{YS} = 616-689 MPa at room temperature and σ_{YS} = 507-577 MPa at 550 ºC.

Keywords ferritic, martensitic steel, microstructural stability, mechanical property, particle coarsening

1. Introduction

Reduced activation ferritic/martensitic (RAFM) steels with a Cr content of 9-12 wt.% (weight percent) have shown great potential as candidate structural materials for lead-cooled fast reactor (LFR) claddings due to their excellent high-temperature (HT) mechanical properties, good thermal conductivity, low thermal expansion, as well as outstanding radiation resistance (Ref 1-4). A well-known HT9 F/M steel (Fe-0.2C-12Cr-1Mo-0.5W-0.5Ni-0.25V, wt.%) has been widely applied in both thermal power boilers and fast reactors (Ref 5, 6). In order to accommodate severe environments, several RAFM steels, such as F82H (Fe-0.09C-8Cr-1.96W-0.15V-0.1Si-0.023Ta, wt.%) (Ref 7, 8), Euorfer97 (Fe-0.11C-8.7Cr-1W-0.19V-0.004Si-0.1Ta-0.44Mn, wt.%) (Ref 9, 10), EP823 (Fe-0.18C-12Cr-0.8Ni-0.9Mo-1.3Si-0.4Nb-0.4V-0.8Mn, wt.%) (Ref 11), and 9Cr2WVTa (Fe-0.1C-8.71Cr-2.17W-0.23V-0.19Si-0.06Ta-0.39Mn, wt.%) (Ref 12), have been developed, in which the active elements of Mo, Nb, Ti, and Cu were replaced with reduced-active W, Ta, V, and Mn elements. This kind of steels shows a similar microstructure with $M_{23}C_6$ and MC carbides distributed in the martensitic matrix after normalizing and tempering treatments, leading to a higher tensile strength at both room and elevated temperatures (Ref 13-15). For instance, fine $M_{23}C_6$ and MC carbide particles (25-210 nm) were uniformly distributed in the martensitic matrix with a width of about 0.5μm in tempered Euorfer97 steel, which renders this alloy with prominent mechanical properties (high yield strength of σ_{YS} = 653 MPa and a large ductility of δ = 21% at room temperature (RT); σ_{YS} = 291 MPa and δ = 32% at 600 ºC) (Ref 16, 17). Actually, the Cr amount should be increased to further improve corrosion and oxidation resistances at HTs, which inevitably accompanies with the increase of C for obtaining single martensitic matrix, such as HT9 (Ref 18). However, an excessive addition of C could accelerate the formation of coarse $Cr_{23}C_6$ carbides, resulting in a reduction of mechanical strength (Ref 19). Thus, the Si element was added to overcome this disadvantage since Si reacts with the oxygen to form dense SiO_2 oxide layers, which plays a similar role to the Cr from the viewpoint of corrosion and oxidation resistances. A series of high-Si RAFM steels were then developed, as exampled by the

Sen Ge, Ben Niu, Zhenhua Wang, and **Qing Wang**, Key Laboratory of Materials Modification By Laser, Iron and Electron Beams (Ministry of Education), School of Materials Science and Engineering, Dalian University of Technology, Dalian 116024 Liaoning, China; and **Qianfu Pan** and **Chaohong Liu**, Science and Technology on Reactor Fuel and Materials Laboratory, Nuclear Power Institute of China, Chengdu 610213 Sichuan, China. Contact e-mails: panqianfu1234@163.com and wangq@dlut.edu.cn.

EP823 steel containing the Si content of about 1.2 wt.% (Ref 11). It is emphasized that the HT δ-Fe ferrite would like to exist in such high-Si F/M steels, leading to a serious embrittlement, especially the HT creep embrittlement (Ref 20). Therefore, the amounts of Cr, C, and Si elements should be tuned to an optimal matching for both the formation of single martensitic matrix and the improvement of resultant mechanical properties.

The microstructural stability of RAFM steels at HTs is crucial to guarantee mechanical properties, especially the HT strength for suppressing the creep. Unfortunately, the $Cr_{23}C_6$ particles are susceptible to be coarsened when the temperature is higher than 600 °C, which would widen the martensitic laths simultaneously. Typically, the $Cr_{23}C_6$ carbide particles in Fe-0.2C-11.5Cr-0.55Ni-0.55Mn-1Mo-0.5W-0.25V-0.6Si (wt.%) martensitic steel were fine with a size of about 100 nm after a short-term (25 h) aging at 650 °C, but they would be coarsened seriously with a size of 0.5-1 μm with prolonging the aging time up to 400 h, leading to the reduction of alloy strength from 731 to 540 MPa (Ref 11). Consequently, the reduced-active elements of W, V, and Ta were added to improve the microstructural stability of F/M steels, as evidenced by the fact that particle size of $M_{23}C_6$ carbides in Fe-0.14C-11.71Cr-2.16W-0.2V-0.09Ta-0.5Si-1.16Mn (wt.%) steel increases slightly from $\sim$ 108 nm after 20 h aging to $\sim$ 148 nm after 500 h aging at 650 ºC (Ref 21). In addition, it is worth nothing that after a long-term (300 h) aging at 650 ºC, the MX carbonitride in Fe-11.85Cr-1.29Ni-0.076Nb-0.183V-0.061N-0.4Si-0.32Mn (wt.%) steel could transform to another intermetallic compound Cr(V/Ta/Nb)N (i.e., *Z* phase), which should be avoided because of its faster coarsening rate (Ref 22) And the reduction of creep-resistant strength in 11-12% Cr F/M steels is primarily ascribed to the appearance of *Z* phase (Ref 23, 24). Moreover, it has been demonstrated that the precipitation of Fe_2(Ta, Nb) Laves phase particles in martensitic matrix is not conducive to the HT microstructural stability and mechanical property of the CLAM steel (Fe-0.09C-8.9Cr-1.51W-0.15V-0.04Si-0.15Ta-0.49Mn (wt.%)) after a long-term aging at 600 °C (Ref 25). Hence, the amounts of reduced-active elements should also be controlled to achieve an optimal combination.

In the present work, an optimized RAFM steel with high Cr and medium Si is designed with the composition range shown in Table 1 after considering both the oxidation/corrosion resistances and microstructural stability at HTs, in which the amounts of alloying elements are matched appropriately to achieve the precipitation of only $Cr_{23}C_6$ and TaC carbides in a single martensitic matrix. Then, the microstructural evolution of the designed alloy with aging temperature and time will be investigated, in which the variations of prior austenite grains, martensitic lath, and precipitated particles are especially focused on. The coarsening of carbide particles at different temperatures will also be discussed. Besides, the mechanical properties of this designed alloy at both room and elevated temperatures will be studied.

2. Experimental

The designed alloy ingot with a weight of 500 kg was prepared by double vacuum melting (vacuum induction + vacuum arc). Then, it was homogenized at 1100 °C for 2 h, followed by hot forging into an alloy rod with a diameter of 15 mm at 850 °C. Subsequently, the rod samples were normalized at 1100 ºC for 1 h to obtain lath martensitic matrix, and then tempered at 700 °C for 1 h to precipitate second-phase particles. Finally, these tempered samples were aged at both 550 and 650 °C for 5, 10, 20, 50, 100, 200, 300, and 500 h, respectively, to investigate the thermal stability of microstructures (especially the prior austenite grains, martensitic laths, and precipitated particles). Each heat treatment was followed by water quenching.

For the alloy rod, its measured composition was measured by the XRF-1800 x-ray fluorescence spectrometer (XRF) (as shown in Table 1), and it was found that the measured composition is within the range of the designed alloy. And then phase equilibria were investigated by means of JMatPro 7.0 software, in which the database for steels was used in the calculation. The microstructures were observed by the Zeiss Supra55 scanning electron microscopy (SEM) with an etchant solution of 1% trinitrophenol + 5% alcohol hydrochloric acid + 94% alcohol (volume fraction). The elemental distributions and phase compositions in heat-treated samples were analyzed by the JXA-8530F PLUS electronic probe micro-analyzer (EPMA). The microstructures were further examined using the JEM-2100F FEG transmission electron microscope (TEM) to further determine the precipitated phase structures, for which the samples were prepared by mechanical polishing down to about 40 μm thickness and then the twin-jet electro-polishing in a solution of 10% perchloric acid + 90% alcohol (volume fraction) at about −30 °C. Microhardness tests were conducted using the HVS-1000 Vickers hardness apparatus under a constant load of 300 g for 15 s, where each sample was tested at least for ten times. Uniaxial tensile tests at room and elevated temperature (550 °C) were conducted on an UTM5504 Material Test System (MTS) equipped with a muffle furnace. And the three tensile samples have a gauge size of 9.0 × 66.0 mm (diameter × length) (room temperature) and 5.0 × 46.0 mm (diameter × length) (550 °C) for each heat-treated state were measured with a strain rate of 1.5 mm/min.

3. Results

3.1 Microstructural Characterization After Normalizing and Tempering Treatments

Figure 1 shows the equilibrium phase fraction as a function of temperature of the designed alloy by the JMatPro 7.0 software. It is found that in the temperature range of

Table 1 Nominal composition range and its measured composition (wt.%) of the designed RAFM steel

	Fe	C	Cr	W	Ta	V	Si	Mn	N
Nominal	Bal.	0.19-0.22	11.8	1.5	0.13-0.15	0.21	0.40-0.61	0.41-0.45	0.013-0.017
Measured	Bal.	0.21	11.76	1.41	0.17	0.20	0.63	0.51	0.015

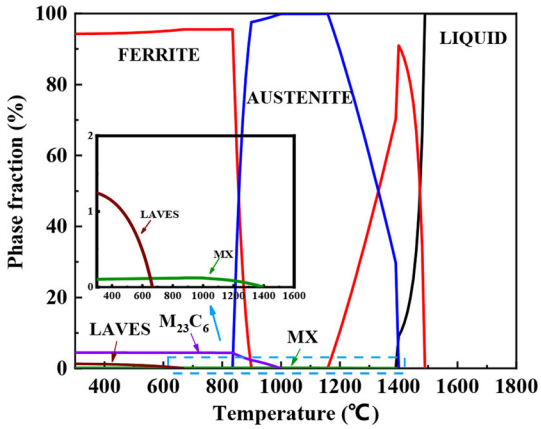

Fig. 1 Variation of equilibrium phases with the temperature in Fe-0.21C-11.76Cr-1.41W-0.17Ta-0.2V-0.63Si-0.51Mn-0.015N steel

900 ~ 1150 °C, the austenite is dominant without any ferrite, which would transform into a full martensitic matrix after water quenching. In addition, the MC-type carbide is very stable in the whole temperature range, where the phase fraction keeps constant from 400 to 1400 °C, being about 0.12% (as seen in the inset of Fig. 1). By contrast, the phase fraction of $M_{23}C_6$ is relatively high (~ 4.4%) below 835 °C and drops drastically to zero when the temperature reaches at 1100 ºC. There also exists Fe_2M Laves phase at low temperatures (< 700 °C) in the equilibrium state. But no other carbides such as M_7C_6 and M_6C are found.

Microstructural observations on the tempered samples with SEM and TEM are presented in Fig. 2, from which it is found that the matrix consists of the martensite alone and the grain size of prior austenite is about 22 ± 8 μm (Fig. 2a). Thus, the normalization at 1100 °C is appropriate for achieving the full martensitic matrix, which is in a well consistence with the calculated result. After tempering at 700 °C for 1 h, both

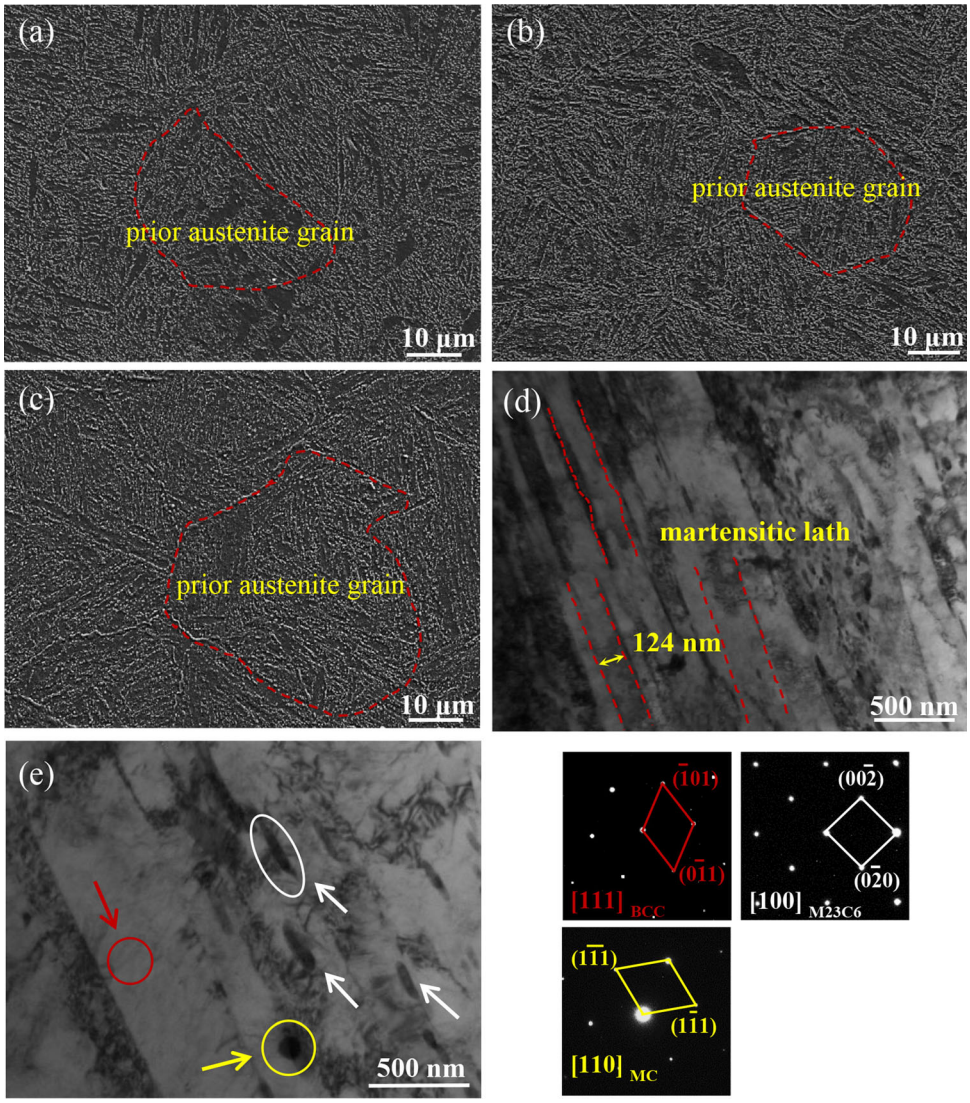

Fig. 2 SEM (a-c) and TEM (d, e) images of the designed alloy in different states. (a, d, e): tempered state, (b): 550 ºC/500 h-aged state, and (c): 650 ºC/500 h-aged state

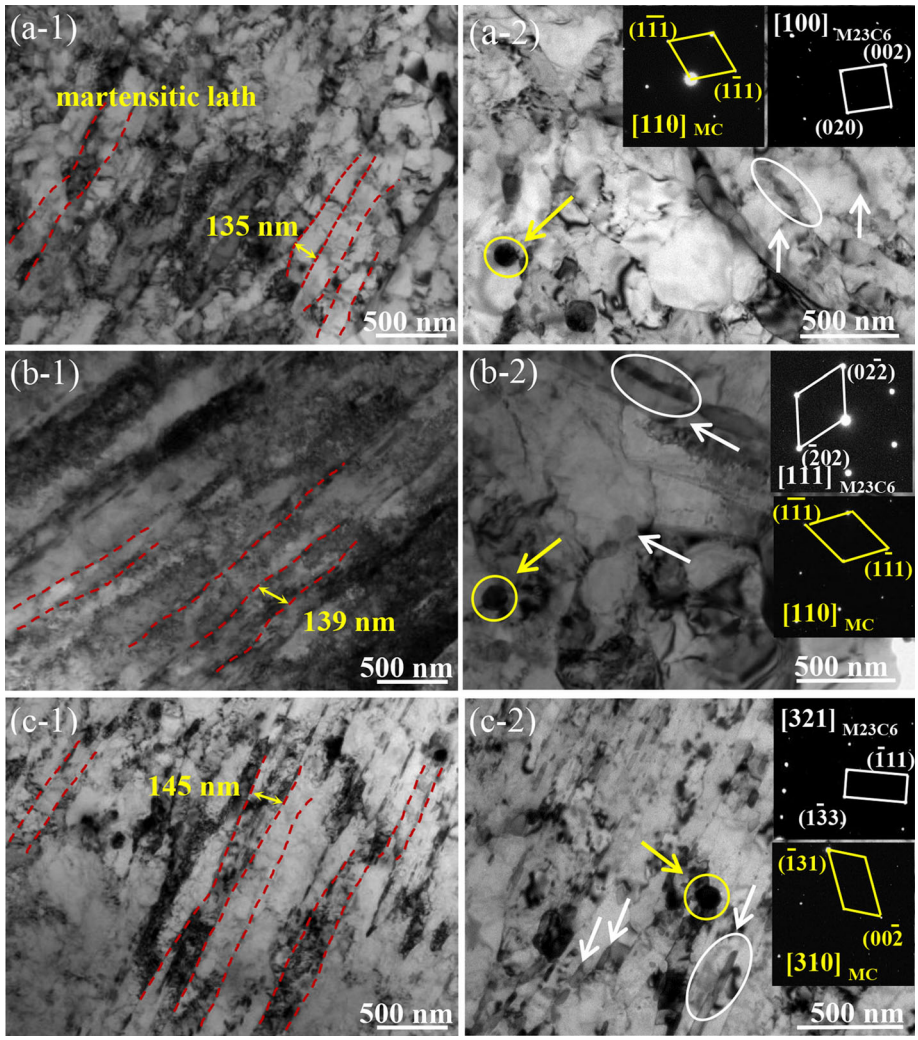

Fig. 3 TEM characterization of 550 ºC-aged alloy for different times. (a-1)-(c-1): martensitic laths, and (a-2)-(c-2): carbide particles for 20 h, 300 h, and 500 h, respectively, in which the lath width of martensite is also marked

$Cr_{23}C_6$ and MC carbides are dispersed uniformly in the martensitic matrix, as evidenced by the TEM bright-field (BF) images and selected-area electron diffraction (SAED) patterns in Fig. 2(d, e). Specifically, the $Cr_{23}C_6$ particles tend to be distributed on the lath boundaries of martensite with a short-rod shape and with a face-centered-cubic (FCC) structure (the lattice constant a = 1.036 nm), in which the average size of $Cr_{23}C_6$ particles is about 132 nm in length and 32 nm in width. While the MC carbide particles are spherical with a size of about 92 nm (in diameter) and distributed in the inner laths, still exhibiting a FCC structure with a = 0.432 nm. And the lath width of body-centered-cubic (BCC) martensite is about 124 ± 21 nm, as seen in Fig. 2(e). In this state, the volume fraction of carbides ($Cr_{23}C_6$ and MC) is about f = 4.7 ± 0.4%.

3.2 Microstructural Evolution During Aging at 550 and 650 ºC

In order to study the thermal stability of microstructures at elevated temperatures, the tempered alloy samples were aged at both 550 and 650 °C for different times of 5 ~ 500 h. It is found that the long time of 500 h aging at 550 °C does not change the prior austenite grains, in which the grain size (~ 22 μm) is comparable to that in tempered state, as seen in Fig. 2(b). Meanwhile, the martensitic laths are not coarsened even after 300 h aging and the lath width increases slightly from 139 ± 29 nm to 147 ± 39 nm when aged for 500 h, as presented in Fig. 3(a-1)-(c-1). Figure 3(a-2)-(c-2) gives the morphologies of carbide particles in 550 °C-aged samples for 20 h, 300 h, and 500 h. It could be seen that the particle sizes of both $Cr_{23}C_6$ and MC carbides keep almost constant with prolonging the aging time, being 155 ± 89 nm and 112 ± 35 nm, respectively. Moreover, no other precipitated phases appear during the aging process.

By contrast, there exists an obvious variation in microstructure during aging at 650 °C. Firstly, the grain size of prior austenite increases up to ~ 40 μm after 500 h aging, as seen in Fig. 2(c). More importantly, the martensitic laths are widened drastically, as evidenced by the fact that the lath width increases from ~ 124 nm in tempered state to ~ 184 nm after 20 h aging, and then to ~ 207 nm and ~ 275 nm after 300 h and 500 h aging, respectively (Fig. 4(a-1)-(c-1)). Also, the $Cr_{23}C_6$ particles are coarsened with the particle size increasing up to ~ 240 nm (in length) after 500 h aging. But the MC particles are not affected by the aging time, and the particle size is about 92-115 nm, as presented in Fig. 4(a-2)-(c-2). Moreover, there does not exist any other precipitated phases even after 500 h aging,

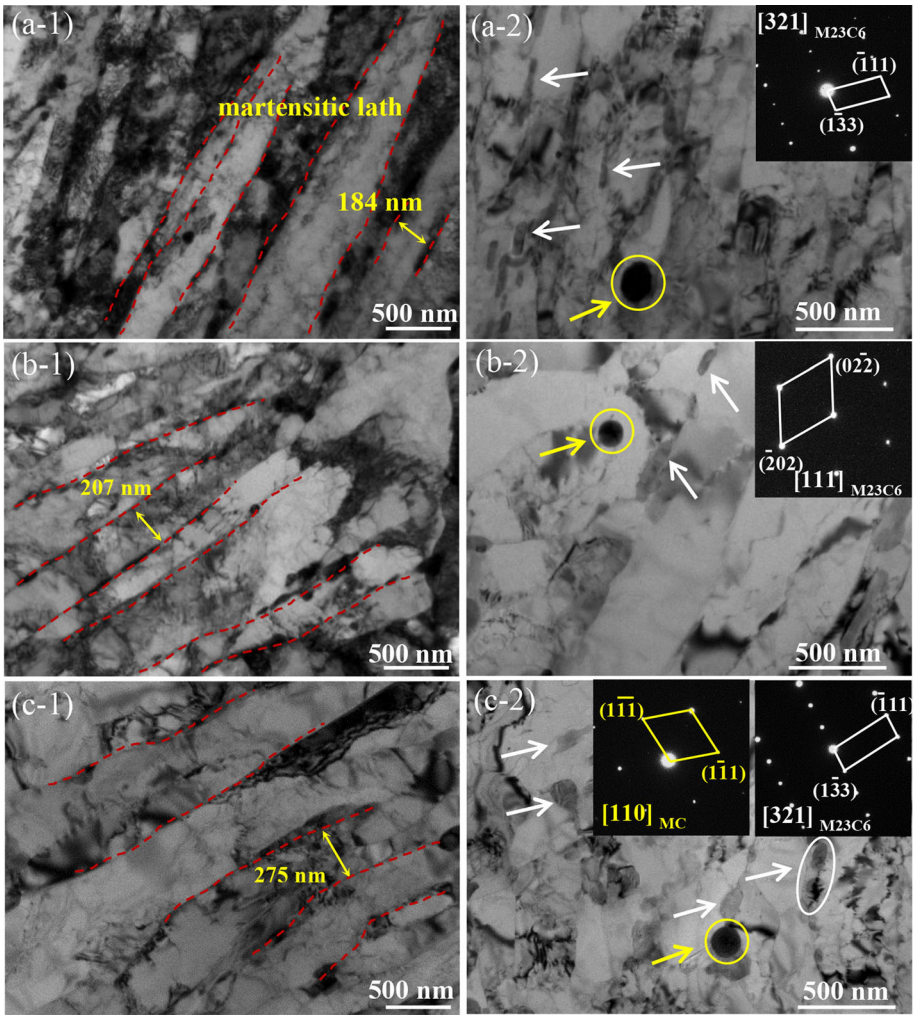

Fig. 4 TEM characterization of 650 ºC-aged alloy for different times. (a-1)-(c-1): martensitic laths, and (a-2)-(c-2): carbide particles for 20 h, 300 h, and 500 h, respectively

similar to that in 550 °C-aged state. The elemental distributions in 500 h-aged sample was analyzed with EPMA (Fig. 5), from which the Cr, W, and C elements are all segregated on grain boundaries of prior austenite obviously, while the Ta element is enriched in the inner grains together with C. It indicates that the $Cr_{23}C_6$ carbide is also enriched with the W element, and the MC carbide could be determined as TaC. Si is uniformly distributed in the martensitic matrix, except in the carbides.

3.3 Mechanical Properties

The microhardness (*HV*) values of aged samples in different states were all measured; the variation of *HV* values with the aging time at both 550 and 650 ºC is shown in Fig. 6(a). It is found that the microhardness value reaches a maximum of ~ 340 *HV* after aging for a short time (20 h) at both 550 and 650 °C. Then, the microhardness value decreases drastically down to ~ 295 *HV* in 50 h-aged state. With furthering increasing the aging time, the microhardness values keep almost constant at 550 °C, while the microhardness would decrease slowly to ~ 280 *HV* after aging for 500 h at 650 °C. This might be ascribed to the fact that the volume fraction of carbides in aged samples reaches the maximum in 20 h-aged state, and then with increase in the aging time, the size of both carbides and martensitic laths is coarsened, especially in aged samples at 650 °C, leading to a slightly decrease in *HV*.

In order to clearly reflect the effect of microstructural evolution on the mechanical properties of aged alloys, tensile tests at both RT and 550 °C of alloy samples were then performed, in which three states of samples were selected, being treated after tempering, 550 °C/ 500 h aging, and 650 °C/ 500 h aging, respectively. Figure 6(b) gives the engineering stress–strain curves of theses treated samples, from which the yield strength (σ_{YS}), the tensile strength (σ_{UTS}), and the elongation to fracture (*El*) are measured and listed in Table 2. The property parameters at RT are σ_{YS} = 620-820 MPa, σ_{UTS} = 810-1000 MPa, and δ-20% for these treated samples; and those at 550 °C are σ_{YS} = 500-650 MPa, σ_{UTS} = 550-725 MPa, and *El*-17%, respectively. The decrease in mechanical strength after 500 h aging is closely related to both the coarsening of carbide particles and the broadening of martensitic laths.

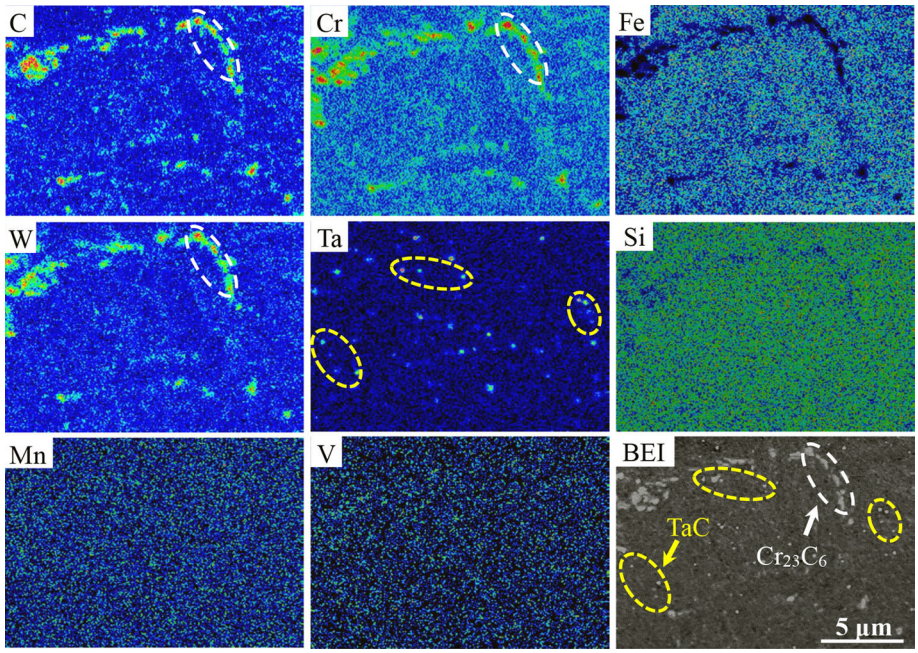

Fig. 5 Elemental distributions in the 650 ºC/ 500 h-aged by the EPMA

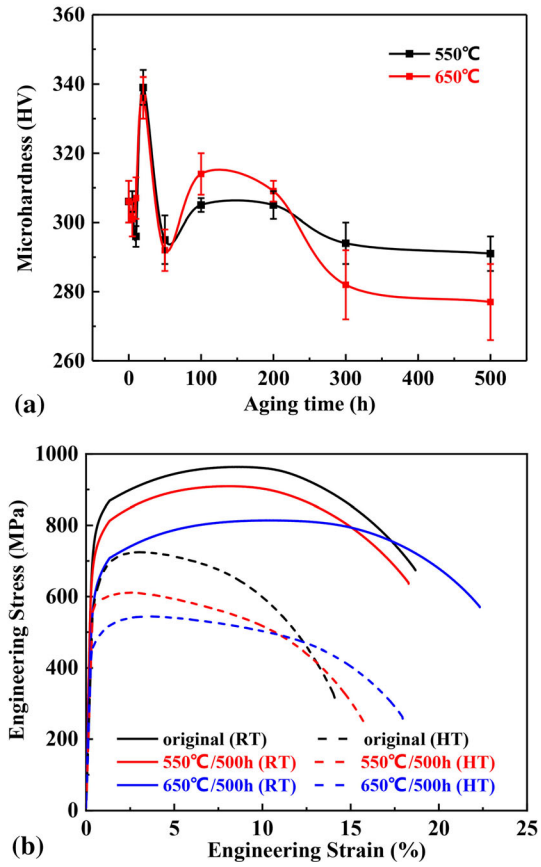

Fig. 6 Mechanical properties of the current alloy in different states, (a): the variation of microhardness *HV* with the aging time at both 550 and 650 ºC, and (b): engineering tensile stress–strain curves measured at room temperature and 550 ºC

4. Discussion

The particle size (the length of $Cr_{23}C_6$ and the diameter of TaC) and volume fraction of carbides, as well as the width of martensitic laths in tempered and aged states were counted. And the variation of these parameters with the aging time at both 550 and 650 °C is presented in Fig. 7. The martensitic laths are very stable during aged at 550 °C, as evidenced by the lath width from 124 ± 21 nm in tempered state to 147 ± 39 nm in 500 h-aged state. However, they are coarsened obviously during aged at 650 ºC with the lath width increasing up to 275 ± 31 nm in 500 h-aged state (Fig. 7a). For the precipitated carbides, the volume fractions in different states are comparable, being 4.7 ± 0.4% in tempered state, 5.2 ± 0.8% in 550 °C/ 500 h-aged state, and 6.8 ± 2.5% in 650 °C/ 500 h-aged state, respectively (Fig. 7b). More importantly, the coarsening of $Cr_{23}C_6$ particles at 650 °C is much faster than that at 550 °C, which could be demonstrated by the fact that length of $Cr_{23}C_6$ particles increases from 132 ± 74 nm in tempered state to 240 ± 36 nm in 650 °C/ 500 h-aged state, while it does not vary during aged at 550 °C with the length of $Cr_{23}C_6$ particles being 155 ± 89 nm after 500 h aging (Fig. 7b). Meanwhile, the spherical TaC particles are very stable during the aging process at these two temperatures and are not coarsened even after a long-term aging with an average size of 92-110 nm (Fig. 7b).

In fact, the coarsening of carbide particles is a significant feature in F/M steels under the operating conditions, which is controlled by the classical Ostwald mechanism (Ref 26). And the Lifshitz–Slyozov–Wanger (LSW) theory was always applied to describe the coarsening behavior of precipitated particles in diverse alloy systems (Ref 27). Thus, the coarsening rate of carbide particles could be obtained by the following Eq. 1 (Ref 28):

Table 2 Tensile property data of the designed alloy in different states measured at room temperature and 550 ºC, including yield strength (σ_{YS}), ultimate tensile strength (σ_{UTS}), and elongation to fracture (*El*)

States	Room temperature			550 °C		
	σ_{YS}, MPa	σ_{UTS}, MPa	*El*,%	σ_{YS}, MPa	σ_{UTS}, MPa	*El*,%
Tempered	818	978	19	657	725	15
550 ºC/500 h	689	909	19	577	611	17
650 ºC/500 h	616	814	22	507	549	19

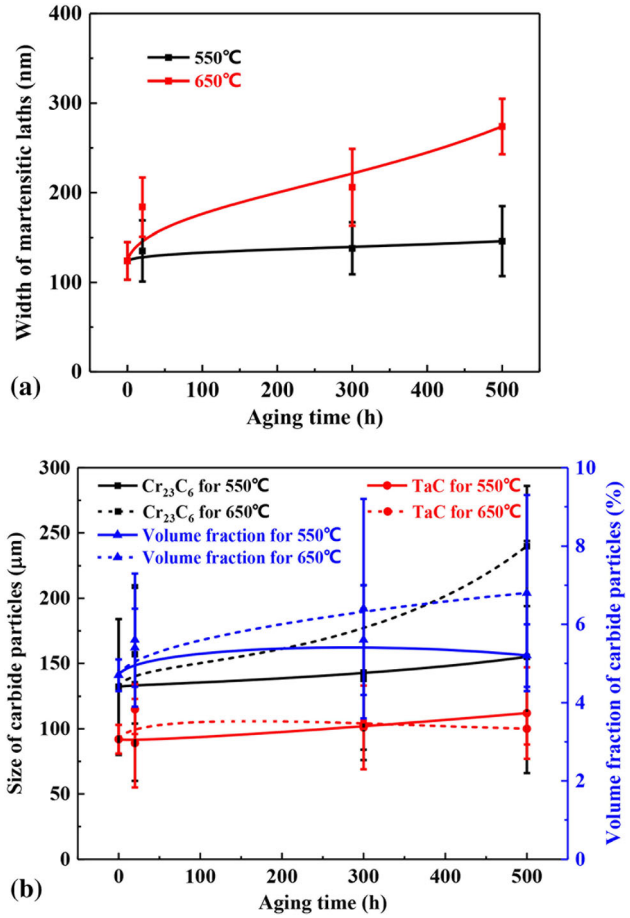

Fig. 7 Variations of the lath width of martensite (a) and the particle size and volume fraction of $Cr_{23}C_6$ and TaC carbides (b) with the aging time at 550 and 650 ºC in the designed alloy

$$r^3(t) - r^3(t_0) = K(t - t_0) \quad \text{(Eq 1)}$$

where K is the coarsening rate constant; $r(t)$ is the average size at time t, which is the half-length for $Cr_{23}C_6$ and the radius for TaC, respectively; and t_0 refers to the time at the onset of coarsening. So the variation of $r^3(t)$ with the time t for both $Cr_{23}C_6$ and TaC particles could be drawn, as presented in Fig. 8, in which the fitted slope is the coarsening rate of particles. Obviously, the coarsening of $Cr_{23}C_6$ particles at both 550 and 650 ºC is much faster than that of TaC particles. TaC particles exhibit a very slow coarsening with K = (1.75-4.52)×10^{-26} m^3/h at these two temperatures. While the coarsening rate constant of $Cr_{23}C_6$ is K = 2.78×10^{-25} m^3/h

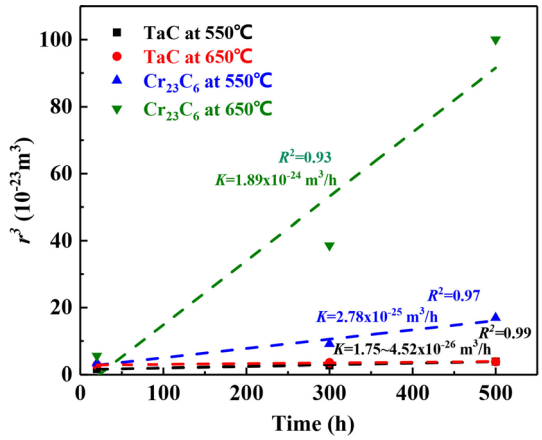

Fig. 8 Plot showing the linear fit of carbides precipitate size vs aging time at 550 and 650 ºC. The coarsening rate constant (K) and coefficient of determination (R^2) were also labeled

at 550 ºC and K = 1.89×10^{-24} m^3/h at 650 ºC, which is about 2-3 orders of magnitude higher than that of TaC particles, indicating that the TaC particles are much more stable than $Cr_{23}C_6$ at elevated temperatures.

It is also emphasized that the particle coarsening is related to the diffusion coefficient of solute elements (Ref 29). Here, the diffusion coefficient values of carbide-forming elements of Cr, Ta, and W in BCC α-Fe at both 550 and 650 ºC were calculated with Eq. 2:

$$D_M = D_O \times \exp(-Q_M/\mathrm{RT}) \quad \text{(Eq 2)}$$

where D_0 is the constant of diffusion coefficient and Q_M is the activation energy of M element for diffusion (Ref 30, 31), R = 8.314 J/mol·K is the gas constant, and T is the Kelvin temperature. The calculated values are listed in Table 3, from which it could be found that the diffusion coefficients of Cr and W elements are much larger than that of Ta at these two temperatures, as evidenced by D_{Cr} = 8.11×10^{-19} m^2/s > D_W = 2.06×10^{-19} m^2/s > D_{Ta} = 8.71×10^{-23} m^2/s at 650 ºC (Ref 32-35). The faster diffusion of Cr and W will lead to a preferably gathering in $Cr_{23}C_6$ and then to a rapid coarsening, which could be well demonstrated by the EPMA result in Fig. 5. By contrast, the lower diffusion coefficient of Ta would certainly result in a slow coarsening rate of TaC particles. In addition, the relatively faster diffusion of carbide-forming elements at 650 ºC accelerates the coarsening of carbide particles, as evidenced by the fact that the particle size of $Cr_{23}C_6$ particles during aging at 650 ºC is much larger than that in 550 ºC-aged state (Fig. 3 and 4).

Table 3 Diffusion data of element M in α-Fe matrix, including the diffusion coefficient prefactor (D_0), the activation energy for diffusion (Q_M), and the diffusion coefficient (D_M)

M	D_0, m^2/s	Q_M, kJ/mol	D^{823K}, m^2/s	D^{923K}, m^2/s
Fe (Ref 33)	4.18×10^{-4}	246.8	9.05×10^{-20}	4.51×10^{-18}
Cr (Ref 33)	5.97×10^{-4}	262.7	1.27×10^{-20}	8.11×10^{-19}
Ta (Ref 34, 35)	2.35×10^{-5}	308	6.64×10^{-25}	8.71×10^{-23}
W (Ref 32)	0.45×10^{-2}	287	2.74×10^{-21}	2.06×10^{-19}

The variation of microstructure (including the lath width of martensite and particle size of carbides) affects the mechanical property of the designed alloy. For the RT yield strength of the present alloy, it exhibits the highest value with σ_{YS} = 818 MPa in tempered state and then decreases gradually down to σ_{YS} = 689 MPa after aging at 550 ºC for 500 h and to σ_{YS} = 616 MPa after aging at 650 ºC for 500 h. The decrease in yield strength is mainly ascribed to both the widening of martensitic laths and the coarsening of carbide particles. It could be identified by the fact that after a long-time (500 h) aging, the width of martensitic lath increases from 124 ± 21 nm in tempered state to 147 ± 39 nm at 550 ºC and to 275 ± 31 nm at 650 ºC, respectively, resulting in a reduction of martensitic matrix strengthening (Ref 36, 37). On the other hand, the length of $Cr_{23}C_6$ increases from 132 ± 52 nm in tempered state to 155 ± 89 nm in 550 ºC/ 500 h-aged state and to 240 ± 36 nm in 650 ºC/ 500 h-aged state obviously, which also contributes to the reduction in yield strength (Ref 38, 39).

5. Conclusions

The microstructural stability at HTs and the mechanical property of Fe-0.21C-11.76Cr-1.41W-0.17Ta-0.2V-0.63Si-0.51Mn-0.015N (wt.%) alloy have been investigated systematically. After tempering, the designed alloy exhibits a full martensitic structure with the lath width of ∼ 139 nm. The martensitic laths are very stable during aged at 550 ºC and the lath width (130-150 nm) does not vary during the aging process, while an obviously widening appears in martensitic laths when aged at 650 ºC with a lath width of about 275 nm in 500 h-aged state. For the precipitated carbides, the TaC particles are very stable during the aging process at both temperatures, as evidenced by the average size of 90-110 nm even after a long-term aging. By contrast, the length of $Cr_{23}C_6$ particles increases distinctly from ∼132 nm in tempered state to ∼ 240 nm in 650 ºC/ 500 h-aged state. The coarsening rate constant ($K = 1.89\times10^{-24}$ m^3/h) of $Cr_{23}C_6$ at 650 ºC calculated by the LSW theory is much higher than that ($K = 4.52\times10^{-26}$ m^3/h) of TaC, which is mainly due to the different diffusion coefficients of carbide-forming elements of Cr and Ta. In addition, the 500 h-aged alloy exhibits prominent mechanical properties at both room temperature (σ_{YS} = 616-689 MPa and *El* = 19-22%), and at 550 ºC (σ_{YS} = 507-577 MPa and *El* = 17-19%).

Acknowledgments

It was supported by the National Natural Science Foundation of China [U1867201], Natural Science Foundation of Liaoning Province of China (2019-KF-05-01).

References

1. J. Vanaja, K. Laha, M. Nandagopal, S. Sam, M.D. Mathew, T. Jayakumar, and E.R. Kumar, Effect of Tungsten on Tensile Properties and Flow Behaviour of RAFM Steel, *J. Nucl. Mater.*, 2013, **433**, p 412–418
2. T. Allen, J. Busby, M. Meye, and D. Petti, Materials Challenges for Nuclear Systems, *Mate. Today.*, 2010, **13**, p 14–23
3. R.L. Klueh, Reduced-Activation Steels: Future Development for Improved Creep Strength, *J. Nucl. Mater.*, 2008, **378**, p 159–166
4. R.J. Kurtz, A. Alamo, E. Lucon, Q. Huang, and J.W. Rensman, Recent Progress Toward Development of Reduced Activation Ferritic/Martensitic Steels for Fusion Structural Applications, *J. Nucl. Mater.*, 2009, **386**, p 411–417
5. H. Yan, X. Liu, L.F. He, and J. Stubbins, Phase Stability and Microstructural Evolution in Neutron-Irradiated Ferritic-Martensitic Steel HT9, *J. Nucl. Mater*, 2021, **557**, p 153252
6. C. Zheng, J.H.K.S.A. Maloy, and D. Kaoumi, Correlation of In-situ Transmission Electron Microscopy and Microchemistry Analysis of Radiation-Induced Precipitation and Segregation in Ion Irradiated Advanced Ferritic/Martensitic Steels, *Scr. Mater.*, 2019, **162**, p 460–464
7. S. Kano, H.L. Yang, R. Suzue, Y. Matsukawa, Y. Satoh, H. Sakasegawa, H. Tanigawa, and H. Abe, Precipitation of Carbides in F82H Steels and its Impact on Mechanical Strength, *Nucl. Mater. Energy*, 2016, **9**, p 331–337
8. G. Ermile, G. Ferenc, S. Ildiko, G. Michael, R. Michael, and D. Eberhard, Development of EUROFER97 Database and Material Property Handbook, *Fusion Eng. Des.*, 2018, **135**, p 9–14
9. M. Klimenkov, U. Jntsch, M. Rieth, and A. Mslang, Correlation of Microstructural and Mechanical Properties of Neutron Irradiated EUROFER97 Steel, *J. Nucl. Mater.*, 2020, **538**, p 152231
10. Z. Yao, C. Liu, and P. Jung, Diffusion and Permeation of Deuterium in EUROFER97: Effect of Irradiation and of Implanted Helium, *Fusion Sci. Technol.*, 2005, **48**, p 1285–1291
11. K.V. Almaeva, I.Y. Litovchenko, and N.A. Polekhina, Microstructure, Mechanical Properties and Fracture of EP-823 Ferritic/Martensitic Steel After High-Temperature Thermomechanical Treatment, *Russ. Phys. J.*, 2020, **63**, p 803–808
12. C. Liu, Q. Shi, W. Yan, C. Shen, K. Yang, Y. Shan, and M. Zhao, Designing a High Si Reduced Activation Ferritic/Martensitic Steel for Nuclear Power Generation by Using Calphad Method, *J. Mater. Sci. Technol.*, 2019, **35**, p 266–274
13. Y.T. Xu, W. Li, M.J. Wang, X.Y. Zhang, Y. Wu, N. Min, W.Q. Liu, and X.J. Jin, Nano-sized MX Carbonitrides Contribute to the Stability of Mechanical Properties of Martensite Ferritic Steel in the Later Stages of Long-Term Aging, *Acta Mater.*, 2019, **175**, p 148–159

14. L. Tan, T.S. Byun, Y. Katoh, and L.L. Snead, Stability of MX-type Strengthening Nanoprecipitates in Ferritic Steels Under Thermal Aging, Stress and Ion Irradiation, *Acta Mater.*, 2014, **71**, p 11–19
15. Y. Xu, Y. Nie, M. Wang, W. Li, and X. Jin, The Effect of Microstructure Evolution on the Mechanical Properties of Martensite Ferritic Steel During Long-Term Aging, *Acta Mater.*, 2017, **131**, p 110–122
16. E. Materna-Morris, A. Möslang, and H.C. Schneider, Tensile and Low Cycle Fatigue Properties of EUROFER97-Steel After 16.3 dpa Neutron Irradiation at 523, 623 and 723 K, *J. Mater. Sci. Technol.*, 2013, **442**, p 62–66
17. X. Chen, A. Bhattacharya, M.A. Sokolov, L.N. Glowers, Y. Yamamoto, T. Graening, K.D. Linton, Y. Katoh, and M. Rieth, Mechanical Properties and Microstructure Characterization of Eurofer97 Steel Variants in EUROfusion Program, *Fusion Eng. Des.*, 2019, **146**, p 2227–2232
18. C. Zheng, M. Stuart, and K. Djamel, Effect of Dose on Irradiation-Induced Loop Density and Burgers Vector in Ion-Irradiated Ferritic/Martensitic Steel HT9, *Philos. Mag.*, 2018, **98**, p 2440–2456
19. A. Puype, L. Malerba, N.D. Wispelaere, R. Petrov, and J. Sietsma, Effect of W and N on Mechanical Properties of Reduced Activation Ferritic/Martensitic EUROFER-based Steel Grades, *J. Nucl. Mater.*, 2018, **502**, p 282–288
20. C. Schroer, V. Koch, O. Wedemeyer, A. Skrypnik, and J. Konys, Silicon-Containing Ferritic/Martensitic Steel after Exposure to Oxygen-Containing Flowing Lead-Bismuth Eutectic at 450 and 550 ºC, *J. Nucl. Mater.*, 2016, **469**, p 162–176
21. X. Xiang, G. Liu, B. Hu, J.S. Wang, and W.B. Ma, Microstructure Stability of V and Ta Microalloyed 12%Cr Reduced Activation Ferrite/Martensite Steel During Long-term Aging at 650 ºC, *J. Mater. Sci. Technol.*, 2015, **3**, p 311–319
22. L. Cipolla, H.K. Danielsen, D. Venditti, P. Nunzio, J. Hald, and M. Somers, Conversion of MX Nitrides to Z-Phase in a Martensitic 12% Cr Steel, *Acta Mater.*, 2010, **58**, p 669–679
23. H.K. Danielsen, and J. Hald, On the Nucleation and Dissolution Process of Z-phase Cr(V, Nb)N in Martensitic 12%Cr Steels, *Mater. Sci. Eng. A.*, 2009, **505**, p 169–177
24. C.G. Panait, W. Bendick, A. Fuchsmann, A.F. Gourgues-Lorenzon, and J. Besson, Study of the Microstructure of the GRADE 91 Steel After More than 100,000 h of Creep Exposure at 600 ºC, *Int. J. Press Vessels Pip.*, 2010, **87**, p 326–335
25. L. Huang, X. Hu, C. Yang, W. Yan, F. Xiao, Y. Shan, and K. Yang, Influence of Thermal Aging on Microstructure and Mechanical Properties of CLAM Steel, *J. Nucl. Mater.*, 2013, **443**, p 479–483
26. C.J. Kuehmann, and P.W. Voorhees, Ostwald Ripening in Ternary Alloys, *Metall. Mater. Trans. A.*, 1996, **27**, p 937–943
27. J.L. Li, Z. Li, Q. Wang, C. Dong, and P.K. Liaw, Phase-Field Simulation of Coherent BCC/B2 Microstructures in High Entropy Alloys, *Acta Mater.*, 2020, **197**, p 10–19
28. F. Perrard, A. Deschamps, and P. Maugis, Modelling the Precipitation of NbC on Dislocations in α-Fe, *Acta Mater.*, 2007, **55**, p 1255–1266
29. H. Nitta, T. Yamamoto, R. Kanno, K. Takasawa, T. Iida, Y. Yamazaki, S. Ogu, and Y. Iijima, Diffusion of Molybdenum in α-iron, *Acta Mater.*, 2002, **50**, p 4117–4125
30. K. Mannesson, J. Jeppsson, A. Borgenstam, and G. John, Carbide Grain Growth in Cemented Carbides, *Acta Mater.*, 2011, **59**, p 1912–1923
31. S. Peter, Analytical Description of Phase Coarsening at High Volume Fractions, *Acta Mater.*, 2013, **61**, p 5026–5035
32. S. Takemoto, H. Nitta, Y. Iijima, and Y. Yamazaki, Diffusion of Tungsten in α-iron, *Philos. Mag.*, 2007, **87**, p 1619–1629
33. C.G. Lee, Y. Iijima, T. Hiratani, and K. Hirano, Diffusion of Chromium in α-Iron, *J. Clin. Microbiol.*, 1990, **31**, p 255–261
34. S.Y. Huang, D.L. Worthington, M. Asta, V. Ozolins, G. Ghosh, and P.K. Liaw, Calculation of Impurity Diffusivities in α-Fe Using First-Principles Methods, *Acta Mater.*, 2010, **58**, p 1982–1993
35. Q.A. Shaikh, Interdiffusion Measurement of Niobium and Tantalum in Iron Base Alloys, *J. Mater. Sci. Technol.*, 1990, **6**, p 1177–1180
36. L. Cho, P.E. Bradley, D.S. Lauria, M.L. Martin, and A.J. Slifka, Characteristics and Mechanisms of Hydrogen-Induced Quasi-Cleavage Fracture of Lath Martensitic Steel, *Acta Mater.*, 2021, **206**, p 116635
37. W.C. Zhong, N. Sridharan, D. Isheim, K.G. Field, Y. Yang, K. Terrani, and L.Z. Tan, Microstructures and Mechanical Properties of a Modified 9Cr Ferritic-Martensitic Steel in the As-Built Condition After Additive Manufacturing, *J. Nucl. Mater.*, 2021, **545**, p 152742
38. D.A. Skobir, M. Godec, A. Nagode, and M. Jenko, Study of the Carbide Coarsening During the Annealing of X20CrMoV12 1 Steel, *Surf. Interface Anal.*, 2010, **42**, p 717–721
39. H.K. Kim, J.W. Lee, J. Moon, C.H. Lee, and H. Hong, Effects of Ti and Ta Addition on Microstructure Stability and Tensile Properties of Reduced Activation Ferritic/Martensitic Steel for Nuclear Fusion Reactors, *J. Nucl. Mater.*, 2018, **500**, p 327–336